Proton emission in Au+Au collisions at 6, 8, and 10.8 GeV/nucleon

B. B. Back,[1] R. R. Betts,[1,5] J. Chang,[3] W. C. Chang,[3,*] C. Y. Chi,[4] Y. Y. Chu,[2] J. B. Cumming,[2] J. C. Dunlop,[7,†] W. Eldredge,[3] S. Y. Fung,[3] R. Ganz,[5,‡] E. Garcia,[6] A. Gillitzer,[1,§] G. Heintzelman,[7,†] W. F. Henning,[1,‖] D. J. Hofman,[1,¶] B. Holzman,[5,†] J. H. Kang,[9] E. J. Kim,[9] S. Y. Kim,[9] Y. Kwon,[9] D. McLeod,[5] A. C. Mignerey,[6] M. Moulson,[4,**] V. Nanal,[1,††] C. A. Ogilvie,[7,‡‡] R. Pak,[8,†] A. Ruangma,[6] D. E. Russ,[6,§§] R. K. Seto,[3] P. J. Stanskas,[6] G. S. F. Stephans,[7] H. Q. Wang,[3,‖‖] F. L. H. Wolfs,[8] A. H. Wuosmaa,[1] H. Xiang,[3] G. H. Xu,[3] H. B. Yao,[7] and C. M. Zou,[3,¶¶]

(E917 Collaboration)

[1]*Argonne National Laboratory, Argonne, Illinois 60439*
[2]*Brookhaven National Laboratory, Upton, New York 11973*
[3]*University of California, Riverside, California 92521*
[4]*Columbia University, Nevis Laboratories, Irvington, New York 10533*
[5]*University of Illinois at Chicago, Chicago, Illinois 60607*
[6]*University of Maryland, College Park, Maryland 20742*
[7]*Massachusetts Institute of Technology, Cambridge, Massachusetts 02139*
[8]*University of Rochester, Rochester, New York 14627*
[9]*Yonsei University, Seoul 120-749, South Korea*

(Received 11 July 2002; published 11 November 2002)

Transverse mass spectra of protons emitted in Au+Au collisions at beam energies of 6, 8, and 10.8 GeV/nucleon have been measured as a function of collision centrality over a rapidity range $0.5<y_{lab}<1.5$. The spectra are well reproduced by Boltzmann distributions over the measured transverse mass region, which allows for extrapolation of the data to derive the rapidity density and apparent temperature of the emitting source. The shapes of the rapidity distributions suggest significant transparency or substantial longitudinal expansion in even the most central collisions at all three beam energies. The data are analyzed within a simple thermal source plus longitudinal expansion model.

DOI: 10.1103/PhysRevC.66.054901 PACS number(s): 25.75.−q, 13.85.Ni, 21.65.+f

I. INTRODUCTION

The possibility that laboratory experiments can re-create the quark-gluon plasma (QGP) [1] has sparked an intense interest in relativistic heavy-ion collisions where the high temperatures and/or density required to produce the QGP may be achieved. This state of matter is believed to have existed during the early stages of the universe until 50 μs after the Big Bang. The aim of the present work is to study the hot interaction region created in such collisions using the proton spectra, since these provide insight into the degree of stopping and consequently indicate the amount of energy deposition in the collision.

Fixed target experiments with beam kinetic energies of $\sqrt{s_{NN}}=1.5$–20 GeV/nucleon have been carried out at the alternating gradient synchrotron (AGS) and the super proton synchrotron (SPS) at CERN. These studies have recently been extended to $\sqrt{s_{NN}}=20$–200 GeV/nucleon at the relativistic heavy-ion collider (RHIC) at Brookhaven National Laboratory. At the lower beam energies it is expected that regions with very high baryon density and moderate temperatures are formed in central heavy-ion collisions. This requires, however, that a large degree of stopping is achieved in the collision, such that the initial beam energy is converted efficiently to compressional energy, thermal motion, and particle production in the system.

A number of prior studies have addressed this question for lighter and/or mass asymmetric systems (see Ref. [2] and references therein) and found that the nuclear stopping is incomplete even for central collisions. In the present work we have studied fixed target Au+Au collisions at beam kinetic energies of 6, 8, and 10.8 GeV/nucleon provided by the AGS. The degree of stopping in the collisions is assessed by studying the emission spectra of protons as a function of rapidity and transverse mass. Since the majority of protons

*Present address: Institute of Physics, Academia Sinica, Taipei 11529, Taiwan.
†Present address: Brookhaven National Laboratory, Upton, NY 11973.
‡Present address: Max Planck Institut für Physik, D-80805, München, Germany.
§Present address: Kernforschungzentrum Jülich, Jülich, D-52425, Germany.
‖Present address: Gesellschaft für Schwerionenforschung, D-64291 Darmstadt, Germany.
¶Present address: University of Illinois at Chicago, Chicago, IL 60607.
**Present address: Laboratori Nationali di Frascati dell'INFN, 00044 Frascati RM, Italy.
††Present address: Tata Institute of Fundamental Research, Colaba, Mumbai 400005, India.
‡‡Present address: Iowa State University, Ames, IA 50011.
§§Present address: National Institute of Health, Gaithersburg, MD 20892.
‖‖Present address: CW Associates, 7676 Woodbine, Markham L3R 2N2, Ontario.
¶¶Present address: H.-M. Zou, Rabobank Nederland, 245 Park Ave, New York, NY 10167.

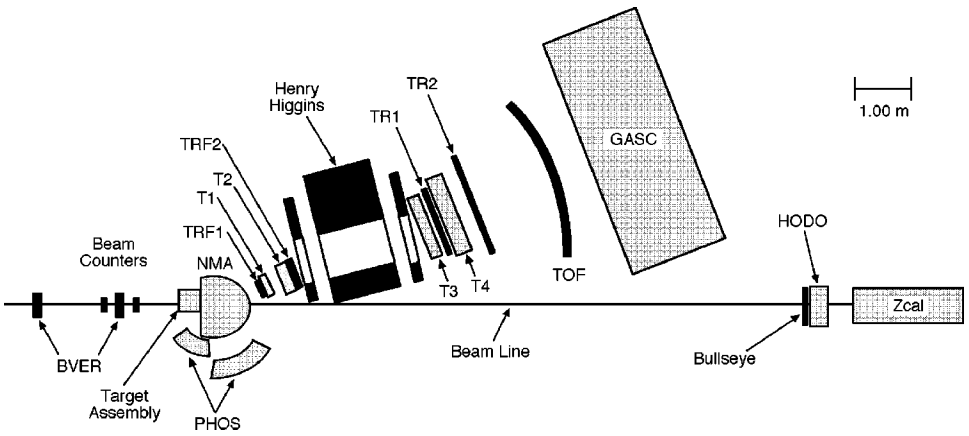

FIG. 1. Schematic view of the E917 experimental apparatus looking down from above showing the beam line detector arrays: the beam vertex detector (BVER); the multiplicity array (NMA); a phoswich array (PHOS); the interaction trigger (Bullseye); a scintillator hodoscope (HODO); the zero-degree calorimeter (ZCAL); and the magnetic spectrometer consisting of a large dipole magnet, multiwire chambers (TRF1,2 and TR1,2), drift chambers (T1–T4), a time-of-flight wall (TOF), and a gas-Čerenkov detector (GASC).

originate from the initial Au nuclei taking part in the collision, integration of the total number of protons is close to the number of 158 present in the entrance channel. A Brief Report of some of our results has appeared in Ref. [3].

In Sec. II we describe the experimental arrangement and data analysis. The measured data are presented in Sec. III and analyzed using Boltzmann distributions for the transverse mass spectra. In Sec. IV we discuss the resulting rapidity distributions and apparent temperatures in terms of a comparison to the expected emission pattern from both a stopped thermal source and a simple model of a continuum of longitudinally distributed sources with a Gaussian temperature profile. Finally, a summary is given in Sec. V.

II. EXPERIMENTAL DETAILS

Au+Au collisions at beam kinetic energies of 6, 8, and 10.8 GeV/nucleon (corresponding to projectile momenta of 6.8, 8.9, and 11.7 GeV/c per nucleon, respectively) were measured during the heavy-ion running period at the Brookhaven AGS in the fall of 1996. This was the final experiment in the series E802/E859/E866/E917. A subset of the apparatus from E866 [4,5] was used, shown schematically in Fig. 1. Global event characterization was achieved with a series of beamline detector arrays, and the large rotatable magnetic spectrometer was used to track and identify particles.

The Au projectiles bombarded an Au target of areal density 1961 mg/cm^2, which corresponds to $\sim$4% interaction probability. A target of areal density 975 mg/cm^2, corresponding to a 2% interaction probability, was also used at 10.8 GeV/nucleon for the large angle settings of the spectrometer. The intensity of the Au beam was kept below a few $\times 10^5$ particles per beam spill, which have a typical duration of 1 s.

Several detectors placed upstream of the target were used to characterize the incident beam. The signal obtained from a thin quartz Čerenkov detector provided a start signal for the time-of-flight measurement. This counter was also used to reject beam contaminants with $Z<76$, and pile-up events occuring within 0.5 μs. A plastic scintillator with a 1 cm hole for the beam to pass through was used to reject beam halo particles. In order to obtain good directional definition of the beam particles two pairs of orthogonally oriented scintillating fiber detectors (BVER) [6] were mounted at distances of 5.84 m and 1.72 m upstream of the target position.

The interaction trigger was obtained from a ''Bullseye'' detector centered on the beam-line 10.6 m downstream of the target. This detector consisted of a 0.3 mm thick, 200 mm diameter Čerenkov radiator viewed by eight photomultiplier tubes. An interaction was defined by observing a signal corresponding to less than $Z=74$ in this detector in coincidence with the signal from the beam counter. The interaction trigger defined in this way selects the most central $\sim$5.1 b of the 6.8 b total interaction cross section. The difference is due to the most peripheral events not being selected by this trigger. The contribution from backgrounds to the interaction cross section was measured by removing the target at regular intervals during the data taking. The background contribution to the interaction trigger was found to be negligible.

The centrality of each event for 6 and 8 GeV/nucleon was obtained from the charged particle multiplicity registered in the new multiplicity array (NMA) consisting of 346 modules arranged around the target in 14 rings at laboratory angles of $112°>\theta>7°$ corresponding to pseudorapidity range of $-0.4<\eta<2.8$ [$\eta=-\ln\tan(\theta/2)$]. Each ring covers a pseudorapidity range of between $\Delta\eta=0.2$ and $\Delta\eta=0.4$ units and the full array covers a solid angle of $\Delta\Omega=6.85$ sr. Multiplicity distributions obtained with this device for 6 and 8 GeV/nucleon are shown in Fig. 2. The boundaries between the five centrality bins (adjusted for each run) are indicated and labeled according to the percentage of the total cross section under the assumption that the collision centrality has a monotonic relationship with the observed multiplicity in the NMA detector [7]. Relevant parameters for the centrality bins are listed in Table I.

For the 10.8 GeV data the event centrality was derived from the forward-going spectator energy measured in the zero degree calorimeter (ZCAL), which is an Fe-scintillator

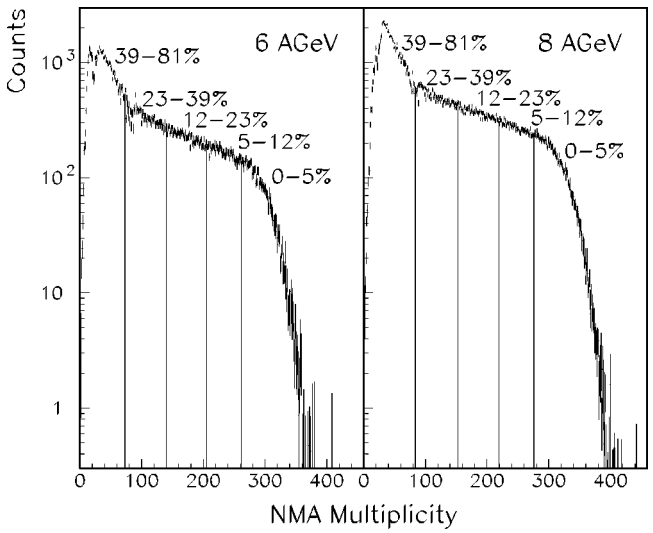

FIG. 2. Measured multiplicity distributions with the NMA from interaction triggers in Au+Au collisions at 6 and 8 GeV/nucleon. Target-out events have been subtracted. The event classes listed in Table I for each beam energy are separated by the vertical lines.

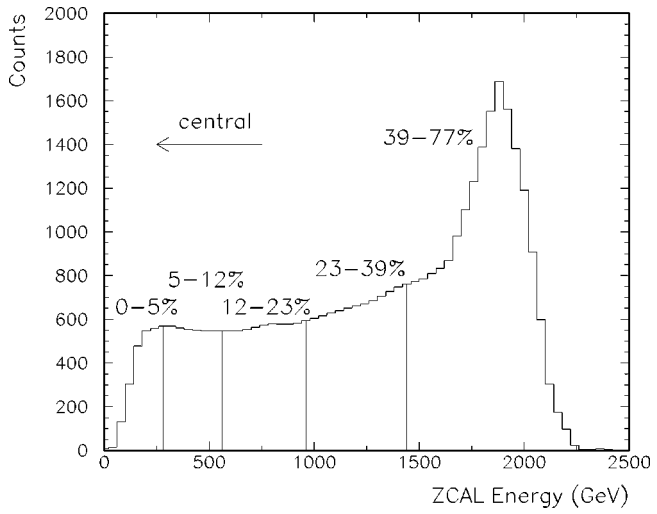

FIG. 3. Measured energy deposition in ZCAL from interaction triggers in Au+Au collisions at 10.8 GeV/nucleon. Target-out events have been subtracted. The event classes listed in Table II are separated by the vertical lines.

sandwich calorimeter subtending an opening angle of 1.5° around the beam axis [8]. The energy calibration of the calorimeter was achieved using the energy deposition from beam particles fragmenting immediately upstream (see Ref. [5]). The energy calibration was adjusted through the 10.8 GeV run for the decrease in signal caused by radiation damage of the plastic scintillator material. The distribution of energy deposition in the zero-degree calorimeter is shown in Fig. 3. Assuming a monotonic relation between the energy deposition in the calorimeter and the event centrality such that the most central events corresponds to the smallest energy deposition, we have divided the distribution into five centrality bin labeled by the corresponding percentage of the total cross section [9]. Relevant parameters for each centrality bin are listed in Table II.

Charged particles were measured in a magnetic spectrometer that provides particle identification and momentum determination. It consists of a large-gap magnetic dipole with sets of drift and multiwire ionization chambers located on both the entrance and exit side of the magnet. These are followed by a time-of-flight (TOF) wall consisting of 160 vertical scintillator slats, each of which was instrumented with a photomultiplier tube on each end. The 17 slats furthest from the beam axis were not in operation during this experiment. The measured overall time resolution of the TOF wall was $\sigma \approx 130$ ps. The momentum range for identified particles is $0.5 < p < 5.0$ GeV/c ($\Delta p/p \approx 1.5\%$). The data presented in this paper were taken with a trigger that required one track in the spectrometer (SPEC). This trigger was formed by a coincidence between any hit in a multiwire chamber (TR1 in Fig. 1) behind the magnet and any hit in the TOF wall. The inefficiency of this trigger was determined to be less than 1%. The spectrometer also has on-line particle identification capability, but this level two trigger was not used to collect the data discussed here.

TABLE I. The five centrality bins used in this paper for 6 and 8 GeV/nucleon collisions, listing the range of multiplicity measured with the NMA, the measured cross section (after target-out correction), and the percentage of the total inelastic cross section ($\sigma_{int} = 6.8$ b) for each centrality bin.

Centrality bin	M_{NMA} range	Cross section (mb)	% σ_{int}
6 Gev/nucleon			
1	>262	0–340	0–5
2	206–262	340–816	5–12
3	140–206	816–1564	12–23
4	73–140	1564–2652	23–39
5	<73	2652–5508	39–81
8 GeV/nucleon			
1	>276	0–340	0–5
2	219–276	340–816	5–12
3	153–219	816–1564	12–23
4	84–153	1564–2652	23–39
5	<84	2652–5508	39–81

TABLE II. The five centrality classes used in this paper for 10.8 GeV/nucleon collisions, listing the measured range of the energy deposited in the ZCAL, the measured cross section (after target-out correction), and the percentage of the total inelastic cross section ($\sigma_{int} = 6.8$ b) for each event class.

Centrality bin	E_{ZCAL} range (GeV)	Cross section (mb)	% σ_{int}
1	0–280	0–340	0–5
2	280–560	340–816	5–12
3	560–960	816–1564	12–23
4	960–1440	1564–2652	23–39
5	>1440	2652–5236	39–77

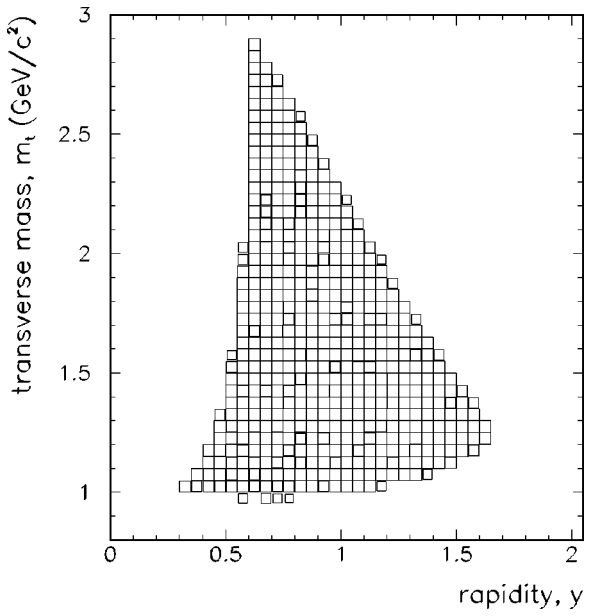

FIG. 4. Combined acceptance for protons in the magnetic spectrometer for angular settings of 14°, 19°, 24°, 29°, 34°, 39°, and 44° and all four settings of magnetic field strength and polarity.

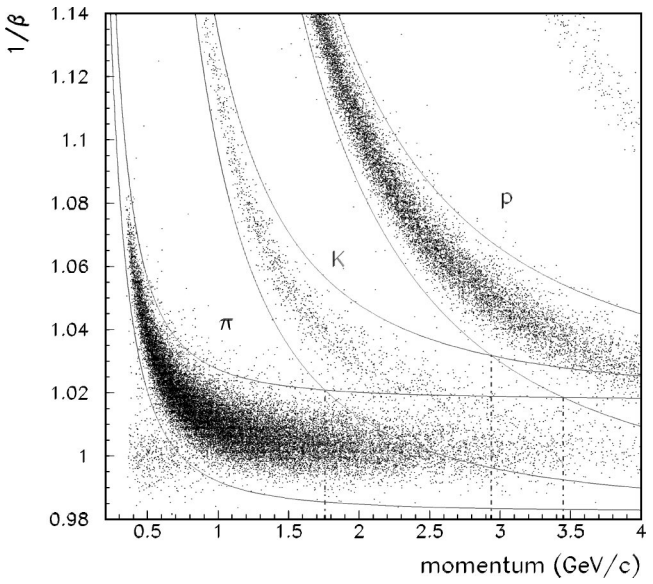

FIG. 5. Scatter plot of inverse velocity versus momentum for the Henry-Higgins spectrometer. The particle identification bands are at $\pm 3\sigma$ in the measured $1/\beta$. The dashed lines denote the limits in momentum for clean separation of pions and kaons, kaons and protons, and pions and protons (see text).

The solid angle of the spectrometer is $\Delta\Omega \approx 25$ msr and it subtends a horizontal opening angle of $\Delta\theta \approx 14°$. Data were taken over the angular range from 14° to 58° by rotating the spectrometer in 5° increments. In order to equalize the acceptance of oppositely charged particles, data were collected with both polarities of the 2.0 kG and 4.0 kG settings of the magnetic field.

The acceptance for protons in the spectrometer is shown in Fig. 4. Particle tracking through the spectrometer was achieved by matching linear track segments generated by charged particles before and after entering the magnetic field region. The efficiency for finding single tracks as a function of their momentum was determined as follows. The detector response to a single Monte Carlo generated track was determined by a GEANT [10] model simulation of the spectrometer including hadronic interactions, decays, and multiple scattering processes. Subsequently, the simulated event was reconstructred using the same tracking and particle identification algorithm that was applied to the real data. Using this procedure we find an efficiency in the range 90–95 % for the the tracking algorithm under the assumption of fully efficient drift chamber detectors. The detection efficiencies of these chambers were in turn found to be very close to 100% on the basis of missing hits in the reconstructed tracks in real data.

Hit blocking caused by the finite occupancy of the gas chambers and the TOF wall also gave rise to loss of tracks. This loss was estimated by embedding hits from isolated single tracks into other events and measuring the fraction of embedded tracks which were not found in a reanalysis of the combined event. For the most central bin with the highest track density, a blocking inefficiency of $40 \pm 10\%$ was found for forward angle tracks declining to $10 \pm 5\%$ at back angles.

A typical particle identification spectrum is shown in Fig. 5, where the inverse particle velocity $1/\beta$ reconstructed from the time-of-flight measurement is plotted versus the momentum of the track. Particle identification is achieved by placing acceptance limits at the $\pm 3\sigma$ level in $1/\beta$ around the loci for each particle species. Using this prescription, we observe that the separation of pions and kaons is effective up to a momentum of $p \approx 1.75$ GeV/c, whereas the separation between pions and protons extends up a momentum of $p \approx 3.4$ GeV/c with a negligible kaon contamination in the proton spectra above $p \approx 2.9$ GeV/c.

Finally, the data were corrected on a track-by-track basis for each inefficiency: single-track reconstruction, chamber inefficiency, loss of tracks due to hit blocking, and particle identification inefficiency.

III. SPECTRA AND YIELDS

Spectra of invariant cross sections for protons, divided by the reaction cross section for the corresponding centrality bin, are shown as a function of transverse mass in ten different rapidity intervals in Fig. 6 for 6 GeV and in Fig. 7 for 10.8 GeV. The 8 GeV data have been published previously in Ref. [3]. The transverse mass is defined as $m_t = \sqrt{p_t^2/c^2 + m_0^2}$, where p_t is the transverse momentum and m_0 is the rest mass of the proton. The data for $0.5 < y < 0.6$ are shown to scale, while the spectrum for each successive rapidity bin is divided by an additional factor of ten in order to avoid overlap. Only statistical errors are shown; these are often smaller than the data points.

Normalization of the data recorded with the SPEC trigger was achieved by the simultaneous recording of prescaled interaction triggered events. The uncertainty of the single-track efficiency and the loss of tracks due to hit blocking dominates the systematic uncertainty on the normalization of the measured invariant spectra. The tracking uncertainty in-

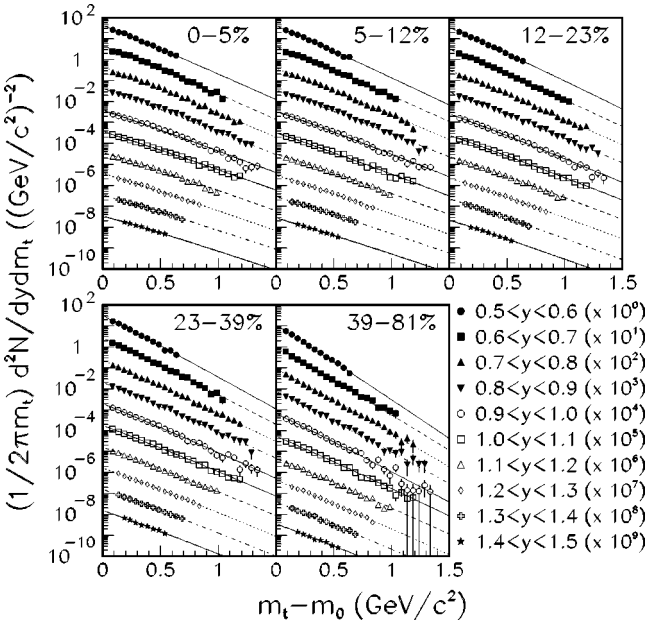

FIG. 6. Invariant yield of protons as a function of transverse mass in ten different rapidity bins for each centrality class of Au+Au collisions at 6 GeV/nucleon. The most backward rapidity in each panel is plotted to scale, while successive spectra have been divided by ten for clarity. The errors are statistical only. The curves are Boltzmann fits described in Sec. III. Systematic errors are discussed in Sec. II.

creases from 5% to 10%, the closer the midrapidity and the more central the event class.

For peripheral collisions, there is a 10% uncertainty in the cross section of the centrality bin, which reduces to 5% for central collisions. In addition, there is a small uncertainty from the acceptance of the spectrometer and particle identification losses. This leads to a total systematic uncertainty of 15%, independent of centrality. The systematic uncertainty on the inverse slope parameters is estimated to be 5% and is dominated by the uncertainty of the tracking efficiency and acceptance.

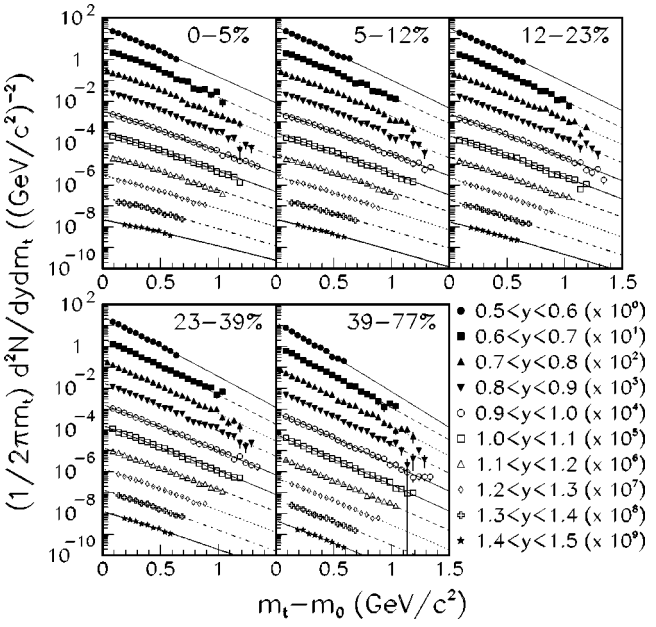

FIG. 7. Same as Fig. 6, but for Au+Au collisions at 10.8 GeV/nucleon.

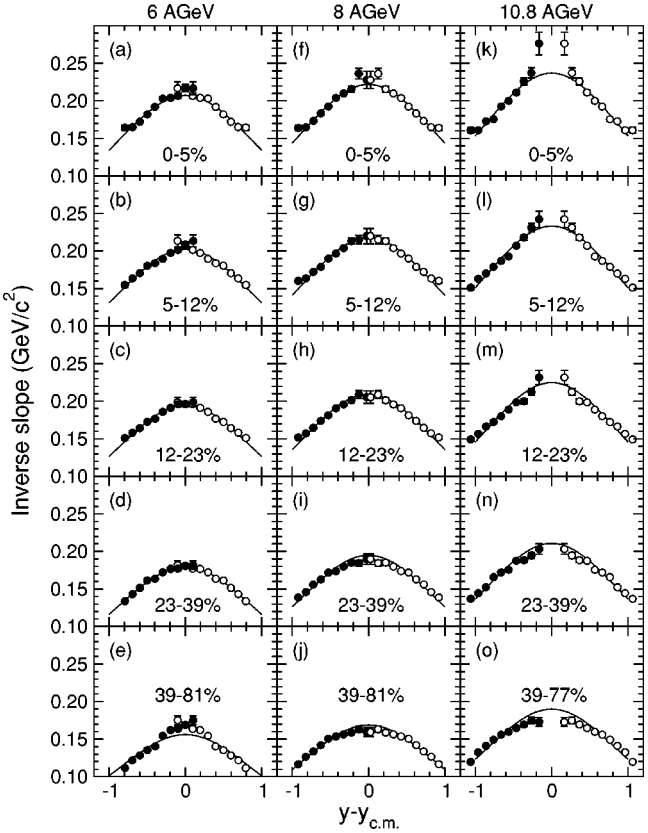

FIG. 8. Inverse slope parameters of protons as a function of rapidity for all centrality classes at all three beam energies from Boltzmann fits to the invariant cross sections. The open symbols are the data reflected about midrapidity. The errors are statistical only.

In Au+Au collisions at 10.8 GeV/nucleon [11], it has previously been found that the proton spectra cannot be satisfactorily described by a simple exponential form. However, using a Boltzmann function,

$$\frac{1}{2\pi m_t}\frac{d^2N}{dm_t dy} = dN/dy\,\frac{m_t e^{-(m_t-m_0)/T}}{2\pi(m_0^2T+2m_0T^2+2T^3)}, \quad (1)$$

and adjusting the parameters T (inverse slope) and dN/dy in a χ^2 fitting procedure with weights related to statistical errors achieves an adequate fit to the data. These Boltzmann fits are shown as curves in Figs. 6 and 7.

The resulting values of the inverse slopes T are shown as a function of the rapidity in the center-of-mass (c.m.) system $y-y_{\mathrm{c.m.}}$ in Fig. 8. The beam rapidity in the c.m. frame is $y_{\mathrm{c.m.}}=1.346$, 1.474, and 1.613 for beam kinetic energy of 6, 8, and 10.8 GeV/nucleon, respectively. The open symbols are the data points reflected about midrapidity. The solid curves in Fig. 8 represent fits using the form $T=T_0/\cosh y$ expected for thermal emission from a fixed source. Although it will be shown below that this assumption is not valid, it is interest-

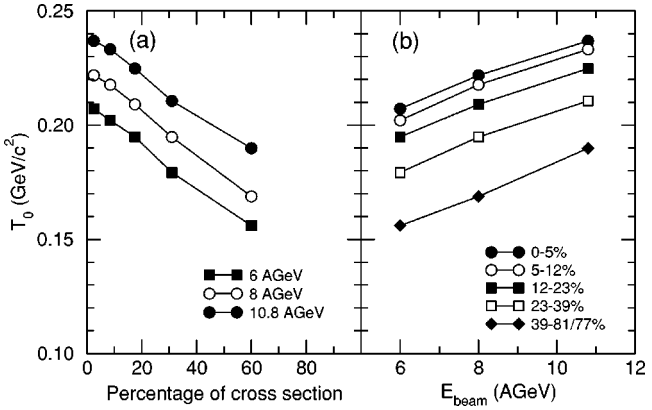

FIG. 9. Fitted values of the T_0 parameter shown as a function of (a) centrality (percentage of cross section) or (b) beam energy.

ing to note that this form quite adequately describes the dependence of the inverse slope T on rapidity in the c.m. system for most centralities. The behavior of the inverse slopes, expressed in terms of the fitted values of T_0 are shown in Fig. 9(a) as a function of centrality (% of cross section). We observe that the inverse slopes (hardness of the m_t spectra) decrease strongly when going to more peripheral collisions and lower beam energies. Figure 9(b) shows that the inverse slopes increase almost linearly with beam energy for all centralities over the region studied here.

Figure 10 shows the centrality dependence of the rapidity density dN/dy as a function of rapidity at each beam energy. The open symbols are the data points reflected about midrapidity. Solid curves represent the best fits with a double Gaussian function that is symmetric about mid rapidity. Unlike the inverse slope parameters, the dN/dy values depend proportionally on the absolute normalization of the m_t spectra. The overall systematic error in the normalization is estimated to be about $\pm(5-10)\%$. However, the error bars shown in Fig. 10 are statistical only and do not reflect this normalization error.

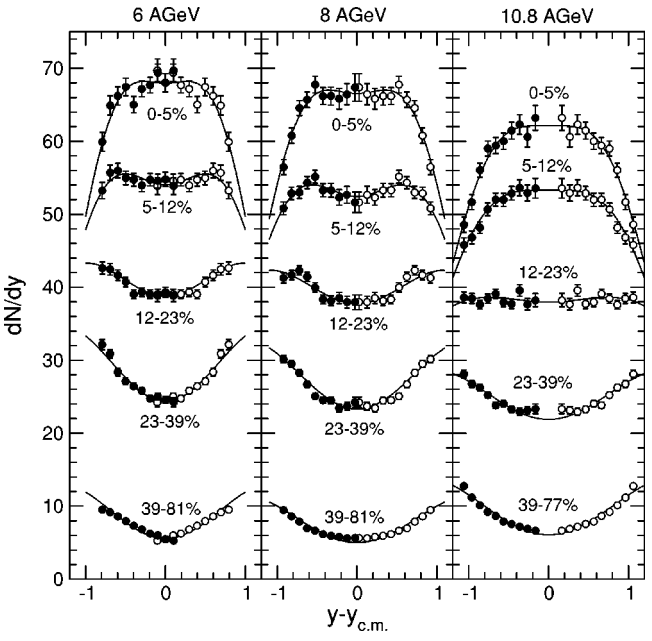

FIG. 10. Rapidity density distributions of protons for all centrality classes at all three beam energy from Boltzmann fits to the invariant cross sections. The open symbols are the data reflected about midrapidity. The errors are statistical only. Systematic errors are described in Sec. II.

The values of dN/dy for the most central event bin at 10.8 GeV/nucleon are in good agreement with the values reported by the E866 Collaboration for the top 5% most central events from Au+Au collisions at the same beam energy [11]. Tables IV, V, and VI in the Appendix list inverse slope, transverse mass, and rapidity density values for each rapidity bin for each centrality class at 6, 8, and 10.8 GeV/nucleon, respectively.

The evolution of the dN/dy distributions with centrality lends strong credence to the conclusion that the wide distributions, even for central collisions, reflect incomplete stopping of the interacting ions. This point is discussed in detail in Ref. [3].

Recently, proton data obtained by the E895 Collaboration at beam energies of 2, 4, 6, and 8 GeV/nucleon for central Au+Au collisions have been published [12]. In a comparison of the dN/dy distributions at 6 and 8 GeV/nucleon with those presented here, we observe a substantial discrepancy between the two data sets that appears to fall somewhat outside the range of values allowed for by the total errors quoted by each experiment. Despite careful assessment of possible systematic error sources by both collaborations, the origin of this discrepancy has not been found.

IV. DISCUSSION OF CENTRAL COLLISIONS

In this section, we compare the dN/dy distributions and mean transverse mass distributions for central collisions with the predictions of three thermal source models, each of increasing complexity. First, it is shown that a single stationary source cannot reproduce the dN/dy distributions, although the transverse mass distributions are well accounted for. Introducing a uniform rapidity boost of isothermal sources can account for the dN/dy distributions, but fails to reproduce the mean transverse masses. Finally, we find that the inclusion of a Gaussian rapidity dependence of the temperature profile in the model gives a remarkably good description of the full data set.

A. A single stationary source

First we compare the measured distributions of protons in the rapidity–transverse-mass plane with the predictions for isotropic emission from a stationary source at midrapidity. It is assumed that a source produced by complete stopping would exhibit this behavior. Guided by the fact that the m_t spectra are well reproduced by a Boltzmann distribution (see Sec. III), we may, furthermore, assume that the emission spectrum exhibits a thermal distribution, i.e.,

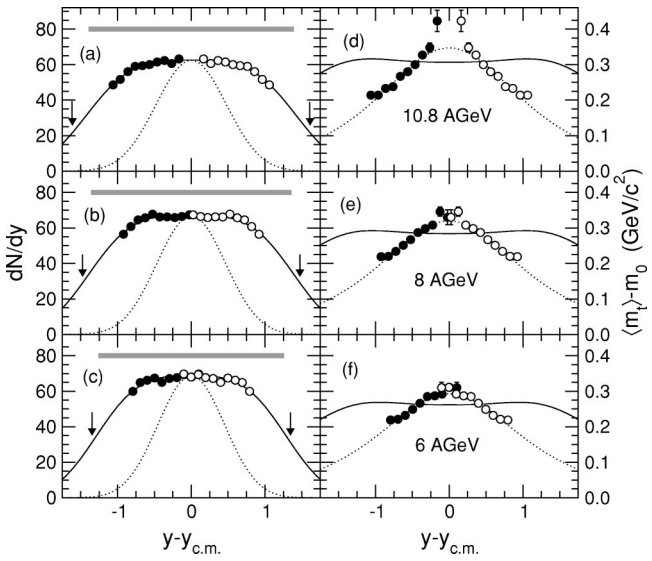

FIG. 11. Proton rapidity distributions in the center-of-mass system (left panels) and average transverse mass (right panels) are compared with a simple thermal source prediction for the three beam energies for the 0–5 % centrality bin. The arrows indicate target and beam rapidities and the solid gray bars represent the rapidity region over which thermal sources are uniformly distributed.

$$\frac{1}{2\pi m_t}\frac{d^2N}{dy\,dm_t} \propto E\exp(-E/T) \tag{2}$$

$$= m_t \cosh y \exp(-m_t \cosh y/T), \tag{3}$$

where y is the rapidity and T is the inverse slope of the spectrum. Although there exists clear evidence that the transverse mass spectra reflect the combined effects of thermal emission and collective expansion, it is an experimental fact that the spectral shapes are very well reproduced by a simple thermal model. As a consequence, the derived inverse slopes do *not* reflect the temperature of the emitting source. In this analysis it is, however, sufficient to require that the emission pattern is isotropic in the center-of-mass system.

We observe that this model predicts a rapidity dependence of the apparent temperature, i.e.,

$$t = T/\cosh y, \tag{4}$$

which, maybe fortuitously, gives an adequate description of the observed inverse slopes (Fig. 8). For a Boltzmann form of the m_t distribution the mean transverse mass is given by

$$\langle m_t \rangle = \frac{m_0^3 + 3m_0^2 t + 6m_0 t^2 + 6t^3}{m_0^2 + 2m_0 t + 2t^2}. \tag{5}$$

In the right-hand panels of Fig. 11 we compare the rapidity dependence of the mean transverse mass $\langle m_t \rangle - m_0$, with those predicted by this model (dotted curves). The apparent source temperature, T, was obtained from a χ^2 fit to the data. We note that this naive model gives a good representation of the observed inverse slopes.

From Eq. (3) we obtain the predicted rapidity distribution for a thermal source by integration

$$\frac{dN_{th}}{dy} \propto \cosh y \int_{m_0}^{\infty} m_t^2 \exp(-m_t \cosh y/T)\, dm_t \tag{6}$$

$$\propto \left(m_0^2 T + 2\frac{m_0 T^2}{\cosh y} + 2\frac{T^3}{\cosh^2 y} \right) \exp(-m_0 \cosh y/T). \tag{7}$$

A comparison of the predicted rapidity distribution with the measurements [dotted curves in Figs. 11(a)–(c)] reveals a discrepancy that clearly demonstrates that the observed proton spectra are inconsistent with isotropic emission from a single source at rest in the center-of-mass system. Rather, we note that the rapidity distributions extend over a wide range of rapidity indicating a significant degree of either incomplete stopping or longitudinal expansion at all three beam energies. Therefore, one may conclude that only a small fraction of the measured protons can originate from such a stopped source; the dotted curves in Fig. 11 thus represent an upper limit for this component (see also Ref. [3]).

A more detailed discussion of the degree of stopping in central Au+Au collisions has been presented [3] in terms of the observed rapidity loss as proposed by Videbæk and Hansen [2]. This analysis also indicates an incomplete degree of stopping in these reactions.

B. Longitudinal expansion

The expanded proton rapidity distributions observed in the present experiment may be interpreted as due to directed longitudinal expansion of the emitting source. From an analysis of the centrality dependence of the dN/dy distributions it is argued [3] that this longitudinal extension is most likely caused by incomplete stopping (transparency) and not by a longitudinal compression and bounce-back mechanism. The longitudinal expansion has sometimes been described [13] in terms of a uniform collection of isothermal sources extending symmetrically over a range of rapidities around midrapidity, i.e.,

$$\frac{dN}{dy} \propto \int_{-\Delta y}^{+\Delta y} \frac{dN_{th}}{dy}(y-\eta)\, d\eta, \tag{8}$$

where Δy is half the total boost range of the thermal sources. This prescription is clearly able to describe the dN/dy distributions for central collisions as illustrated in the left-hand panels of Fig 11 (solid curves). However, it is also a consequence of this model that the m_t-spectra will exhibit nearly constant inverse slopes over this range of rapidity $-\Delta y < y < \Delta y$ (solid curves in right-hand panels of Fig. 11), which is at variance with the data. This point has often been ignored in thermal model analysis of data where the dN/dy proton distributions have been fitted, but the spectral shape of the m_t distributions away from midrapidity has been ignored in the analysis [12]. In fact, this inability to reproduce proton m_t spectral forms away from midrapidity is already clearly visible in Fig. 9 of Ref. [14].

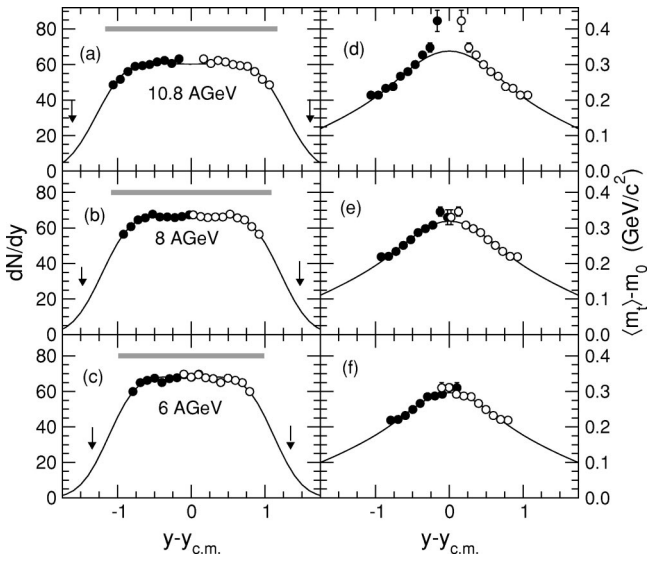

FIG. 12. Measurements (solid) of dN/dy (a)–(c) and mean transverse mass (d)–(f) are compared with optimum fits (solid curves) with a model of isotropically emission from a continuum of thermal sources with a Gaussian temperature profile (see text). The solid gray bars represent the rapidity region over which thermal sources are uniformly distributed. Open circles are data points reflected around midrapidity. Arrows in (a)–(c) indicate the target and beam rapidities in the center-of-mass system.

C. Gaussian temperature profile

In order to obtain a satisfactory representation of the m_t distributions measured away from midrapidity it thus seems necessary to impose a ''temperature'' distribution upon the emitting sources such that the ''hottest'' sources are located at midrapidity and that the ''temperature'' decreases as one goes away from this rapidity. We have illustrated this by assuming a uniform distribution of sources over the range $-\Delta y < y < \Delta y$ which have Gaussian temperature distribution in y, such that

$$\frac{dN}{dy} \propto \int_{-\Delta y}^{+\Delta y} \frac{dN_{th}}{dy}[y-\eta, T(y-\eta)]\, d\eta, \tag{9}$$

TABLE III. Parameters used in model calculations with longitudinally boosted thermal sources for either an isothermal source distribution or a distribution of sources with a Gaussian rapidity distribution for Au+Au collisions. The parameters are: E_{beam}^{kin} the kinetic energy of the beam, T_0 the source temperature at midrapidity, Δy the longitudinal rapidity boost range away from midrapidity, $N = \int_{-\infty}^{+\infty}(dN/dy)dy$ the total thermal source strength integrated over rapidity, and σ_T the standard deviation of the Gaussian temperature distribution.

	Isothermal		Gaussian temperature distribution			
E_{beam}^{kin} (GeV/nucleon)	T_0 (GeV/c^2)	Δy	T_0 (GeV/c^2)	σ_t	Δy	N
6.0	0.207	1.26	0.253	0.696	0.99	155
8.0	0.222	1.36	0.267	0.762	1.086	164
10.8	0.237	1.37	0.280	0.809	1.166	159

TABLE IV. The inverse slope, mean transverse mass, and rapidity density values for each centrality class for 6 GeV/nucleon collisions. The errors are statistical only.

Bin	Rapidity	Inverse slope (GeV/c^2)	$\langle m_t \rangle - m_0$ (GeV/c^2)	dN/dy
1	0.55	0.164±0.004	0.219±0.006	59.9±1.3
1	0.65	0.165±0.002	0.221±0.003	64.9±1.3
1	0.75	0.172±0.001	0.232±0.002	66.2±1.3
1	0.85	0.182±0.002	0.249±0.003	67.4±1.2
1	0.95	0.192±0.002	0.266±0.004	65.0±1.1
1	1.05	0.203±0.003	0.285±0.005	67.2±1.1
1	1.15	0.204±0.003	0.287±0.005	67.7±1.1
1	1.25	0.207±0.003	0.292±0.006	69.4±1.2
1	1.35	0.217±0.005	0.311±0.009	68.0±1.2
1	1.45	0.217±0.008	0.310±0.015	69.7±1.6
2	0.55	0.155±0.003	0.204±0.005	53.2±1.1
2	0.65	0.164±0.002	0.218±0.003	55.7±1.1
2	0.75	0.171±0.001	0.230±0.002	56.0±1.0
2	0.85	0.180±0.002	0.246±0.003	55.0±0.9
2	0.95	0.184±0.002	0.252±0.004	54.7±0.9
2	1.05	0.190±0.002	0.262±0.004	53.9±0.8
2	1.15	0.198±0.002	0.276±0.004	54.7±0.8
2	1.25	0.201±0.003	0.283±0.006	54.6±0.9
2	1.35	0.209±0.004	0.296±0.007	54.8±1.0
2	1.45	0.213±0.008	0.304±0.014	53.9±1.2
3	0.55	0.151±0.003	0.198±0.004	42.6±0.8
3	0.65	0.158±0.002	0.209±0.002	42.5±0.8
3	0.75	0.164±0.001	0.219±0.002	41.6±0.7
3	0.85	0.172±0.002	0.233±0.003	40.7±0.7
3	0.95	0.177±0.002	0.240±0.003	39.0±0.6
3	1.05	0.186±0.002	0.255±0.004	39.3±0.6
3	1.15	0.191±0.002	0.265±0.004	39.1±0.6
3	1.25	0.196±0.003	0.273±0.005	39.1±0.6
3	1.35	0.196±0.004	0.273±0.006	39.3±0.7
3	1.45	0.199±0.006	0.278±0.011	38.9±0.9
4	0.55	0.134±0.002	0.171±0.003	32.1±0.7
4	0.65	0.143±0.001	0.185±0.002	30.9±0.6
4	0.75	0.151±0.001	0.199±0.002	28.4±0.5
4	0.85	0.161±0.002	0.215±0.003	27.1±0.5
4	0.95	0.164±0.002	0.218±0.003	26.4±0.4
4	1.05	0.172±0.002	0.232±0.003	25.8±0.4
4	1.15	0.177±0.002	0.240±0.004	24.8±0.4
4	1.25	0.177±0.003	0.241±0.004	25.0±0.5
4	1.35	0.181±0.003	0.247±0.006	24.6±0.5
4	1.45	0.182±0.006	0.248±0.009	24.2±0.6
5	0.55	0.111±0.002	0.137±0.003	9.5±0.2
5	0.65	0.122±0.002	0.153±0.002	9.2±0.2
5	0.75	0.128±0.001	0.162±0.002	8.6±0.2
5	0.85	0.135±0.002	0.173±0.003	8.0±0.2
5	0.95	0.140±0.002	0.181±0.003	7.3±0.1
5	1.05	0.154±0.002	0.203±0.003	6.8±0.1
5	1.15	0.162±0.002	0.216±0.003	6.2±0.1
5	1.25	0.164±0.003	0.218±0.004	6.0±0.1
5	1.35	0.169±0.003	0.227±0.006	5.5±0.1
5	1.45	0.175±0.006	0.237±0.010	5.2±0.2

TABLE V. The inverse slope, mean transverse mass, and rapidity density values for each centrality class for 8 GeV/nucleon collisions. The errors are statistical only.

Bin	Rapidity	Inverse slope (GeV/c^2)	$\langle m_t \rangle - m_0$ (GeV/c^2)	dN/dy
1	0.55	0.164±0.003	0.219±0.006	56.5±1.0
1	0.65	0.165±0.002	0.220±0.003	60.8±1.1
1	0.75	0.173±0.001	0.234±0.002	64.5±1.0
1	0.85	0.183±0.002	0.251±0.003	65.7±1.1
1	0.95	0.193±0.002	0.267±0.003	67.8±1.2
1	1.05	0.204±0.002	0.287±0.004	66.2±1.2
1	1.15	0.210±0.003	0.298±0.005	66.2±1.2
1	1.25	0.216±0.004	0.308±0.008	65.8±1.4
1	1.35	0.236±0.007	0.346±0.013	66.4±1.5
1	1.45	0.228±0.012	0.330±0.021	67.4±1.9
2	0.55	0.160±0.003	0.213±0.005	50.8±0.9
2	0.65	0.163±0.002	0.218±0.003	52.9±0.9
2	0.75	0.172±0.001	0.233±0.002	53.0±0.8
2	0.85	0.179±0.001	0.244±0.002	54.3±0.9
2	0.95	0.190±0.002	0.263±0.003	55.1±0.9
2	1.05	0.197±0.002	0.274±0.004	53.3±0.9
2	1.15	0.204±0.003	0.287±0.004	53.3±1.0
2	1.25	0.213±0.004	0.304±0.007	52.3±1.1
2	1.35	0.215±0.006	0.307±0.010	52.6±1.2
2	1.45	0.220±0.010	0.316±0.019	51.6±1.4
3	0.55	0.152±0.003	0.199±0.004	41.3±0.7
3	0.65	0.157±0.001	0.208±0.002	41.7±0.7
3	0.75	0.165±0.001	0.220±0.002	42.3±0.6
3	0.85	0.174±0.001	0.235±0.002	41.4±0.6
3	0.95	0.181±0.002	0.248±0.003	40.0±0.6
3	1.05	0.191±0.002	0.264±0.003	38.3±0.6
3	1.15	0.196±0.002	0.273±0.004	38.1±0.7
3	1.25	0.201±0.004	0.282±0.006	38.5±0.8
3	1.35	0.209±0.005	0.296±0.009	38.0±0.8
3	1.45	0.205±0.008	0.290±0.015	37.9±1.0
4	0.55	0.139±0.002	0.178±0.004	30.1±0.5
4	0.65	0.146±0.001	0.190±0.002	29.5±0.5
4	0.75	0.156±0.001	0.206±0.002	28.3±0.4
4	0.85	0.163±0.001	0.217±0.002	26.7±0.4
4	0.95	0.172±0.002	0.232±0.003	25.1±0.4
4	1.05	0.174±0.002	0.235±0.003	24.5±0.4
4	1.15	0.180±0.002	0.245±0.004	24.5±0.5
4	1.25	0.185±0.003	0.254±0.006	23.4±0.5
4	1.35	0.184±0.004	0.253±0.007	23.7±0.6
4	1.45	0.190±0.007	0.262±0.012	24.2±0.7
5	0.55	0.117±0.002	0.145±0.003	9.5±0.2
5	0.65	0.126±0.002	0.160±0.002	8.6±0.2
5	0.75	0.134±0.001	0.170±0.002	7.9±0.1
5	0.85	0.142±0.002	0.184±0.002	7.0±0.1
5	0.95	0.150±0.002	0.197±0.003	6.6±0.1
5	1.05	0.154±0.002	0.202±0.003	6.2±0.1
5	1.15	0.156±0.002	0.206±0.004	5.9±0.1
5	1.25	0.159±0.003	0.210±0.005	5.8±0.2
5	1.35	0.163±0.004	0.217±0.006	5.6±0.2
5	1.45	0.160±0.006	0.212±0.010	5.6±0.2

TABLE VI. The inverse slope, mean transverse mass, and rapidity density values for each centrality class for 10.8 GeV/nucleon collisions. The errors are statistical only.

Centrality bin	Rapidity (GeV/c^2)	Inverse slope (GeV/c^2)	$\langle m_t \rangle - m_0$	dN/dy
1	0.55	0.161±0.004	0.214±0.006	48.6±1.1
1	0.65	0.161±0.002	0.214±0.003	51.7±1.0
1	0.75	0.173±0.002	0.233±0.003	56.0±1.0
1	0.85	0.176±0.002	0.238±0.003	59.0±1.0
1	0.95	0.192±0.002	0.267±0.004	59.4±1.1
1	1.05	0.200±0.002	0.280±0.004	60.0±1.1
1	1.15	0.211±0.003	0.300±0.005	61.5±1.2
1	1.25	0.226±0.005	0.327±0.009	62.3±1.3
1	1.35	0.237±0.007	0.348±0.013	60.6±1.4
1	1.45	0.276±0.015	0.423±0.030	63.2±1.7
2	0.55	0.151±0.003	0.198±0.005	45.8±1.0
2	0.65	0.163±0.002	0.217±0.003	46.8±0.9
2	0.75	0.170±0.002	0.229±0.003	48.2±0.8
2	0.85	0.179±0.002	0.244±0.003	50.7±0.8
2	0.95	0.187±0.002	0.257±0.003	52.0±0.9
2	1.05	0.193±0.002	0.268±0.004	52.0±0.9
2	1.15	0.207±0.002	0.293±0.004	52.9±0.9
2	1.25	0.218±0.004	0.312±0.007	53.6±1.1
2	1.35	0.231±0.006	0.337±0.011	52.9±1.1
2	1.45	0.242±0.011	0.357±0.021	53.6±1.3
3	0.55	0.149±0.003	0.195±0.004	38.6±0.7
3	0.65	0.156±0.002	0.207±0.003	38.5±0.7
3	0.75	0.166±0.002	0.223±0.003	37.6±0.6
3	0.85	0.172±0.002	0.233±0.003	38.4±0.6
3	0.95	0.180±0.002	0.246±0.003	39.1±0.6
3	1.05	0.189±0.002	0.261±0.003	37.9±0.6
3	1.15	0.198±0.002	0.277±0.004	37.7±0.7
3	1.25	0.200±0.003	0.280±0.006	39.6±0.8
3	1.35	0.212±0.005	0.302±0.008	37.7±0.8
3	1.45	0.232±0.009	0.337±0.017	38.2±0.9
4	0.55	0.137±0.002	0.176±0.004	28.1±0.6
4	0.65	0.144±0.002	0.187±0.003	26.7±0.5
4	0.75	0.152±0.001	0.200±0.002	26.3±0.4
4	0.85	0.166±0.002	0.222±0.003	25.2±0.4
4	0.95	0.172±0.002	0.232±0.003	23.8±0.4
4	1.05	0.176±0.002	0.238±0.003	24.0±0.4
4	1.15	0.188±0.002	0.259±0.004	23.3±0.4
4	1.25	0.188±0.003	0.260±0.005	22.9±0.5
4	1.35	0.195±0.004	0.271±0.007	23.1±0.5
4	1.45	0.203±0.007	0.286±0.013	23.3±0.7
5	0.55	0.120±0.002	0.149±0.003	12.7±0.3
5	0.65	0.132±0.002	0.169±0.003	11.2±0.2
5	0.75	0.141±0.002	0.182±0.002	10.1±0.2
5	0.85	0.149±0.002	0.195±0.003	9.2±0.2
5	0.95	0.156±0.002	0.206±0.003	8.7±0.2
5	1.05	0.160±0.002	0.212±0.003	7.9±0.2
5	1.15	0.165±0.002	0.220±0.004	7.6±0.2
5	1.25	0.169±0.003	0.228±0.005	7.2±0.2
5	1.35	0.175±0.004	0.237±0.007	6.9±0.2
5	1.45	0.173±0.006	0.233±0.010	6.6±0.2

$$T(y) = T_0 \exp[-(y - y_{cm})^2 / 2\sigma_T^2], \quad (10)$$

where T_0 is the ''temperature'' of midrapidity sources and σ_T is the standard deviation of the ''temperature'' distribution in rapidity y. That this simple form is able to simultaneously reproduce the dN/dy and the mean transverse mass is shown in Fig. 12. The parameters used are listed in Table III. It is interesting to note that the total number of protons obtained by integration of the calculated dN/dy distributions and listed in Table III accounts quite accurately for the 158 protons available in the entrance channel. This may be significant, since the rate of baryon production in Au+Au collisions at these energies is expected to be insignificant on this scale; the $\bar{p}/p$ ratio is observed to be $\sim 10^{-3}$ [15].

We emphasize that this should not be taken as a definitive model to describe central collisions, but rather to suggest the necessary ingredients required for a more realistic model that includes both thermal and collective expansion effects. Recently, a similar conclusion has been reached by Dobler *et al.* [16] from an analysis of 11.6 GeV/c Au+Au data from the E866 collaboration [5,11] in which the optimum fit to the data is obtained by allowing for a rapidity dependent freeze-out temperature in an asymmetrically expanding thermal source model. Clearly, a more detailed model analysis of the present data is required.

V. CONCLUSIONS

An analysis of m_t spectra for protons emitted in central Au+Au collisions at beam kinetic energies of 6, 8, and 10.8 GeV/nucleon in terms of Boltzmann distributions has been carried out, and the resulting dN/dy distributions and inverse slopes derived. A simple model assuming isotropic emission from a continuum of thermal sources with temperatures that follow a Gaussian dependence on the rapidity gives a remarkably good description of both the rapidity density and mean transverse mass of proton spectra in central collisions.

ACKNOWLEDGMENTS

This work was supported by the U.S. Department of Energy under contracts with ANL (Contract No. W-31-109-Eng-38), BNL (Contract No. DE-AC02-98CH10886), MIT (Contract No. DE-AC02-76ER03069), UIC (Contract No. DE-FG02-94ER40865), and UC Riverside (Contract No. DE-FG03-86ER40271), the National Science Foundation under contracts with University of Rochester (Contract No. PHY-9722606), and the Ministry of Education and KOSEF (Contract No. 951-0202-032-2) in Korea.

APPENDIX

This appendix contains tables of parameters derived from Boltzmann fits the the measured proton spectra (Tables IV, V, and VI). The inverse slope, the mean transverse mass, and the rapidity density dN/dy are listed for ten rapidity bins (in the laboratory system) for each centrality bin.

[1] E.V. Shuryak, Phys. Rep. **61**, 71 (1980); L. McLerran, *ibid.* **88**, 379 (1982).
[2] F. Videbæ and O. Hansen, Phys. Rev. C **52**, 2684 (1995).
[3] B.B. Back *et al.* (E917 Collaboration), Phys. Rev. Lett. **86**, 1970 (2001).
[4] T. Abbott *et al.*, Nucl. Instrum. Methods Phys. Res. A **290**, 41 (1990).
[5] L. Ahle *et al.* (E802 Collaboration), Phys. Rev. C **58**, 3523 (1998).
[6] B.B. Back *et al.*, Nucl. Instrum. Methods Phys. Res. A **412**, 191 (1998).
[7] L. Ahle *et al.* (E802 Collaboration), Phys. Rev. C **59**, 2173 (1999).
[8] D. Beavis *et al.*, Nucl. Instrum. Methods Phys. Res. A **281**, 367 (1989).
[9] B. B. Back *et al.* (E917 Collaboration) (unpublished).
[10] http://www.info.cern.ch/asd/geant/, GEANT 3.2.1, CERN Program Library, W5013 1993.
[11] L. Ahle *et al.* (E802 Collaboration), Phys. Rev. C **57**, R466 (1998).
[12] J.L. Klay *et al.* (E895 Collaboration), Phys. Rev. Lett. **88**, 102301 (2002).
[13] E. Schnedermann, J. Sollfrank, and U. Heinz, Phys. Rev. C **48**, 2462 (1993).
[14] S. Chapman and J.R. Nix, Phys. Rev. C **54**, 866 (1996). In Fig. 9 it is clear that the experimental m_t spectra exhibit substantially smaller inverse slopes than those predicted by the expanding, but isothermal, source model discussed in this paper.
[15] B.B. Back *et al.* (E917 Collaboration), Phys. Rev. Lett. **87**, 242301 (2001).
[16] H. Dobler, J. Sollfrank, and Ulrich Heinz, nucl-th/9904018.